

Article

Structural, Electrical, and Electrochemical Properties of a Na₂O-V₂O₅ Ceramic Nanocomposite as an Active Cathode Material for a Na-Ion Battery

Ahmed Ibrahim ¹, Satoshi Watanabe ¹, Marta Razum ², Luka Pavić ², Zoltán Homonnay ³, Ernő Kuzmann ³, Mohamed Yousry Hassaan ⁴ and Shiro Kubuki ^{1,*}

¹ Department of Chemistry, Graduate School of Science, Tokyo Metropolitan University, Tokyo 192-0397, Japan; elawadyahmed59@gmail.com (A.I.); watanabe-satoshi3@ed.tmu.ac.jp (S.W.)

² Division of Materials Chemistry, Ruđer Bošković Institute, 10000 Zagreb, Croatia; mrazum@irb.hr (M.R.); lpavic@irb.hr (L.P.)

³ Institute of Chemistry, Eötvös Loránd University, 1117 Budapest, Hungary; homonnay.zoltan@ttk.elte.hu (Z.H.); erno.kuzmann@ttk.elte.hu (E.K.)

⁴ Physics Department, Faculty of Science, Al-Azhar University, Nasr City, Cairo 11884, Egypt

* Correspondence: kubuki@tmu.ac.jp

Abstract: In this paper, a relationship between the structure and the electrical properties of a nanocrystalline composite ceramics $x\text{Na}_2\text{O} \cdot (100 - x)\text{V}_2\text{O}_5$ with ‘ x ’ of 5, 15, 25, 35, and 45 mol%, abbreviated as $x\text{NV}$, was investigated by X-ray diffractometry (XRD), X-ray absorption spectroscopy (XAS), Cyclic Voltammetry (CV), Electrochemical impedance spectroscopy (EIS), and cathode active performance in Na-ion battery (SIB). For the expected sodium vanadium bronzes ($\text{Na}_x\text{V}_2\text{O}_5$) precipitation, the preparation of $x\text{NV}$ was performed by keeping the system in the molten state at 1200 °C for one hour, followed by a temperature decrease in the electric furnace to room temperature at a cooling rate of 10 °C min⁻¹. XRD patterns of the 15NV ceramic exhibited the formation of $\text{Na}_{0.33}\text{V}_2\text{O}_5$ and NaV_3O_8 crystalline phases. Moreover, the V K-edge XANES showed that the absorption edge energy of ceramics 15NV recorded at 5479 eV is smaller than that of V_2O_5 at 5481 eV, evidently indicating a partial reduction from V^{5+} to V^{4+} due to the precipitation of $\text{Na}_{0.33}\text{V}_2\text{O}_5$. In the cyclic voltammetry, reduction peaks of 15NV were observed at 1.12, 1.78 V, and 2.69 V, while the oxidation peak showed up only at 2.36 V. The values of the reduction peaks were related to the NaV_3O_8 crystalline phase. Moreover, the diffusion coefficient of Na^+ (D_{Na^+}) gradually decreased from $8.28 \times 10^{-11} \text{ cm}^2 \text{ s}^{-1}$ to $1.23 \times 10^{-12} \text{ cm}^2 \text{ s}^{-1}$ with increasing Na_2O content (x) from 5 to 45 mol%. In the evaluation of the active cathode performance of $x\text{NV}$ in SIB, ceramics 15NV showed the highest discharge capacity 203 mAh g⁻¹ at a current rate of 50 mA g⁻¹. In the wider voltage range from 0.8 to 3.6 V, the capacity retention was maintained at 50% after 30 cycles, while it was significantly improved to 90% in the narrower voltage range from 1.8 to 4.0 V, although the initial capacity decreased to 56 mAh g⁻¹. It is concluded that the precipitation of the $\text{Na}_{0.33}\text{V}_2\text{O}_5$ phase improved the structural and electrical properties of 15NV, which provides a high capacity for the Na-ion battery when incorporated as a cathode active material.

Keywords: crystal structure; sodium-ion battery; XAFS; $\text{Na}_{0.33}\text{V}_2\text{O}_5$ crystalline phase; impedance spectroscopy



Citation: Ibrahim, A.; Watanabe, S.; Razum, M.; Pavić, L.; Homonnay, Z.; Kuzmann, E.; Hassaan, M.Y.; Kubuki, S. Structural, Electrical, and Electrochemical Properties of a Na₂O-V₂O₅ Ceramic Nanocomposite as an Active Cathode Material for a Na-Ion Battery. *Crystals* **2023**, *13*, 1521. <https://doi.org/10.3390/cryst13101521>

Academic Editor: Yutaka Moritomo

Received: 20 September 2023

Revised: 14 October 2023

Accepted: 17 October 2023

Published: 20 October 2023



Copyright: © 2023 by the authors. Licensee MDPI, Basel, Switzerland. This article is an open access article distributed under the terms and conditions of the Creative Commons Attribution (CC BY) license (<https://creativecommons.org/licenses/by/4.0/>).

1. Introduction

Rechargeable sodium-ion batteries (SIBs) would significantly ease and grow the present energy storage industry, primarily based on the lithium-ion battery (LIB) technology [1]. SIBs are a more economical way to LIBs regarding material abundance, allowing their use in high-scale energy storage, such as in smart-grid applications [1]. Among the most common rechargeable batteries (LIBs) used in smartphones and laptops are those

with a total capacity of 3861 mAh g^{-1} [1]. Also, due to the increasing use of Li-ion batteries in the automotive market (vast quantities of lithium are required), SIBs may become the preferred battery for plug-in hybrid electric vehicles (PHEVs), powering hybrid electric vehicles (HEVs) and electric vehicles (EVs) [2]. Nonetheless, the rising costs associated with the rapid increase in demand for lithium [3] and the uneven global distribution of lithium [4] have become a severe problem. Therefore, the development of new secondary batteries is desired.

Recently, many batteries have appeared to use other chemical elements as an alternative to lithium. Many scientists have started searching for other elements that are more abundant in nature and low-priced to be widely used in battery manufacturing. These elements are Ca^{2+} [5], Al^{3+} [6], Mg^{2+} [7], K^+ [8], and Na^+ [9,10]. Sodium is the most abundant of these elements, as it has a practically unlimited supply in the earth's crust and seawater [11]. On the other hand, sodium shows similar properties as lithium because both elements belong to the same group in the periodic table [12,13]. Therefore, sodium-ion batteries (SIB) have been attracting attention because the abundance of lithium in the crust is 20 ppm, while that of sodium is 23,600 ppm, and SIB has a high theoretical capacity of 1166 mAh g^{-1} [1]. Also, despite all the many advantages found in sodium, there are some challenges, as lithium has a lower relative atomic weight (Li: 7 and Na: 23). Also, the radius of the Na-ion is almost twice as large as that of the Li-ion (Li: 0.67 \AA vs. Na: 1.02 \AA), which challenges the improvement of high-performing electrode materials with high energy density [11,12].

Regarding the development of active cathode materials for SIB, Yabuuchi et al. revealed that $\alpha\text{-NaFeO}_2$ had an initial discharge capacity of 100 mAh g^{-1} when utilized as a SIB cathode material [14]. Furthermore, SIB utilizing NASICON-type $\text{Na}_3\text{V}_2(\text{PO}_4)_3$ produced by a simple sol-gel technique for cathode material demonstrated a high initial capacity of 112.5 mAh g^{-1} and capacity retention of 86% after 500 cycles [15]. In addition, Tepavcevic et al. reported that electrodeposited V_2O_5 achieved a discharge capacity of 250 mAh g^{-1} [16]. These studies showed that using vanadium oxide as a cathode material has high potential in SIB.

Vanadium oxides and vanadate, such as V_2O_5 , NaV_3O_8 , and $\text{Na}_{1.1}\text{V}_3\text{O}_{7.9}$, have been extensively investigated as potential electrode materials due to their favorable characteristics, including high capacity, cost-effectiveness, and abundant availability. Recently, there has been a growing interest in $\beta\text{-Na}_{0.33}\text{V}_2\text{O}_5$, distinguished by its robust 3D tunneled structure [17,18]. This 3D tunneled structure exhibits excellent stability compared to layered structures and suggests an efficient pathway for ion diffusion [19]. Researchers, including Bach et al. [20], have delved into studying the (de)intercalation behavior of sodium in $\beta\text{-Na}_{0.33}\text{V}_2\text{O}_5$.

Furthermore, efforts have been made to reduce the particle size of $\beta\text{-Na}_{0.33}\text{V}_2\text{O}_5$ to enhance its electrochemical performance for sodium storage [21]. Despite these endeavors, $\text{Na}_{0.33}\text{V}_2\text{O}_5$ materials still face challenges related to rapid capacity degradation and limited rate performance, which are possibly attributed to self-aggregation and substantial resistance polarization. As a result, there is a growing need for tailored nanoarchitecture and the incorporation of electronically conductive materials. These approaches aim to establish shorter ion diffusion paths and enhance surface conductivity, ensuring prolonged and high-rate cycling performance [22,23].

Vanadium bronze is predicted to be applied as an active cathode material for secondary batteries because it has high electrical conductivity ($10^0\text{--}10^1 \text{ S cm}^{-1}$) [24] and high cycle stability [25]. In addition, the electrical conductivity of vanadium bronze is high compared with other compounds used as cathode material such as $\text{Na}_4\text{ZrSi}_4\text{O}_{12}$ ($1.96 \times 10^{-4} \text{ S cm}^{-1}$) [26], $\text{Na}_{3.5}\text{Cr}_{0.5}\text{Ti}_{1.5}(\text{PO}_4)_3$ ($8.5 \times 10^{-4} \text{ S cm}^{-1}$) [27], and $\text{Na}_{1.5}\text{Al}_{0.5}\text{Ge}_{1.5}\text{P}_3\text{O}_{12}$ ($9.27 \times 10^{-5} \text{ S cm}^{-1}$) [28]. Kubuki et al. reported that the heat treatment of $x\text{Na}_2\text{O} \cdot 10\text{P}_2\text{O}_5 \cdot (90-x)\text{V}_2\text{O}_5$ ($5 \leq x \leq 45 \text{ mol\%}$) glass resulted in a large discharge capacity of 173 mAh g^{-1} recorded under a current density of 5 mA g^{-1} when it was incorporated as a cathode active material for SIB [29]. They concluded that the heat treatment improved the cycle stability by precipitation of

the $\text{NaV}_6\text{O}_{15}$ crystalline phase. In addition, Khan et al. reported that the heat-treated $20\text{CaO}\cdot 10\text{Fe}_2\text{O}_3\cdot 70\text{V}_2\text{O}_5$ glass has a discharge capacity of 138 mAh g^{-1} recorded under a current density of 50 mA g^{-1} [30]. They concluded that the precipitation of $\text{Ca}_{0.17}\text{V}_2\text{O}_5$ called beta-vanadium bronze ($\beta\text{-MxV}_2\text{O}_5$) by heat treatment contributed to the increase in capacity. Based on results obtained by Khan et al. [30], we can expect that in our present study of $\text{Na}_2\text{O}\cdot\text{V}_2\text{O}_5$ ceramics with precipitation of vanadium bronze, high electrical conductivity, and large discharge capacity compared with $x\text{Na}_2\text{O}\cdot 10\text{P}_2\text{O}_5\cdot (90-x)\text{V}_2\text{O}_5$ ($5 \leq x \leq 45 \text{ mol\%}$) [29].

In the present work, we studied a relationship between the local structure and electrochemical properties of $\text{Na}_2\text{O}\cdot\text{V}_2\text{O}_5$ ceramics by X-ray diffractometry (XRD), X-ray absorption spectroscopy (XAFS), Cyclic Voltammetry (CV), Electrochemical impedance spectroscopy (EIS), and the charge–discharge capacity test of the SIB.

2. Materials and Methods

2.1. Preparation

2.1.1. xNV Ceramics

The starting reagents of the ceramics system with the composition $x\text{Na}_2\text{O}\cdot(100-x)\text{V}_2\text{O}_5$ ($5 \leq x \leq 45 \text{ mol\%}$, abbreviated as xNV) were mixed and put into a platinum crucible. The mixtures were melted in an electric muffle furnace at $1200 \text{ }^\circ\text{C}$ and kept there for one hour. Then, the temperature of the electric furnace decreased to room temperature (RT), with a cooling rate of $10 \text{ }^\circ\text{C min}^{-1}$. Raw chemical materials for preparing the ceramics system were Na_2CO_3 (Wako, Osaka, Japan, 199-01585) and V_2O_5 (Wako, Osaka, Japan, 226-00125). Depending on the ratio of Na_2O and V_2O_5 starting materials, various types of sodium vanadate phases are expected to form (even unreacted V_2O_5 in case of insufficient amount of Na_2O). The relatively slow cooling results in microcrystalline composite materials.

2.1.2. Na-Ion Battery

The Na-ion battery was prepared in a 2032-type coin cell, which includes xNV, metallic Na (Kishida, Osaka, Japan, 620-70852), and $1\text{M NaClO}_4/\text{propylene carbonate}$ solution (Tomypure LIPASTE-P/S1, Tokyo, Japan) as a cathode, an anode, and an electrolyte, respectively. For preparing the cathode, 250 mg ceramics sample and 95 mg acetylene black (AB, Strem Chemicals 06-0025, Newburyport, MA, USA) were mixed under 800 rpm for 30 min by a (Planet M2-3F, Nagao System, Kanagawa, Japan). After ball milling, 95 mg of the ball-milled powder sample and 5 mg polytetrafluoroethylene (PTFE, Wako, Osaka, Japan, 165-13412) were mixed to make a pellet with 1 cm in diameter and 30 mg in weight with the mass ratio of xNV to AB to PTFE as 70:25:5. The charge–discharge capacity tests of the SIBs were performed under a current rate of 50 mA g^{-1} and in voltage ranges from 0.8 to 3.6 V, from 1.5 to 4 V, and from 1.8 to 4.0 V at room temperature.

2.2. Material Characterization

X-ray diffractometry was used to determine the crystalline phases of the xNV ceramics. X-rays were generated from Cu K_α with a wavelength of 0.1541 nm by setting the tube voltage and current at 50 kV and 300 mA, respectively. The XRD patterns were measured under the diffraction angle 2Θ range from 10° to 80° and scanning rates $0.02^\circ \text{ min}^{-1}$ and 5° min^{-1} . Crystal phases were analyzed using Smartlab Studio II Powder XRD software, version 4.2.137.0, and the reference data from the International Center for Diffraction Data (ICDD).

Transmission electron microscopy (TEM) images were obtained using a JEM-3200FS Field Emission Energy Filter Electron Microscope (JEOL, Tokyo, Japan).

The Fourier Transform Infrared Spectroscopy (FT-IR) transmission spectra of xNV were recorded by a FT-IR PerkinElmer spectrometer, Shelton, CT, USA; in the wavenumber range from 400 to 1300 cm^{-1} with the resolution of 2 cm^{-1} . For FT-IR measurements, the powder samples were mixed with high-purity KBr and pressed into pellets of 12 mm in diameter under an applied load of 90 kg/mm^2 , with the sample weight ratio of each sample/KBr kept at $\sim 4\%$.

X-ray absorption spectra (XANES/EXAFS) of the V K-edge were measured in transmission mode at the Photon Factory, High Energy Accelerator Research Organization (KEK-PF, 1-1 Oh-ho, Tsukuba, Ibaraki 305-0801, Japan). The X-ray intensity was measured by setting ionization chambers before and after the transmission. The front chamber was filled with He + N₂ gas (He: 70%, N₂: 30%), while the rear was filled with N₂ + Ar gas (N₂: 85%, Ar: 15%). A pellet with a diameter of 1 cm was prepared for measurement by pressing the mixture composed of 5 mg (for V K-edge) and 100 mg boron nitride at 20 kN. The spectra obtained were analyzed by the Athena software version 0.9.26.

Electrical properties were obtained by measuring the complex impedance with an impedance analyzer (Novocontrol Alpha-AN Dielectric Spectrometer, Novocontrol Technologies GmbH & Co. KG, Montabaur, Germany) in a frequency range from 0.01 Hz to 1 MHz at temperatures from -90 °C to 150 °C. The temperature was controlled to an accuracy of ± 0.2 °C. For the electrical measurements, powder samples were compacted into cylindrical pellets with a 5 mm diameter and 1 mm thickness, applying a consistent force of 2×10^3 kg via a hydraulic press. To establish electrical connections, gold electrodes, measuring 3.8 mm in diameter, were deposited on both sides of the disk pellets using a sputter coater SC7620 by Quorum Tech. Electrochemical impedance spectra (EIS) were measured from 0.01 Hz to 100 kHz at room temperature. Cyclic voltammetry (CV) was measured by using (TOSCAT-3100SK, Toyosystem, Fukushima, Japan) at a scan rate of 0.1 mV s^{-1} in the voltage range from 0.8 to 3.6 V at RT. Constant current-constant voltage (CC-CV) conditions were used for charging, and CC measurements were used for discharging.

3. Results and Discussion

3.1. XRD Patterns of *x*NV Ceramics

Figure 1 displays XRD patterns of *x*NV with Na₂O content (*x*) of 5, 15, 25, 35, and 45 mol%. There are sharp peaks between 2θ of 10° and 45° , which can be attributed to crystalline phases; the crystalline phases of *x*NV are summarized in Table 1. The crystalline phase of V₂O₅ (ICDD No. 00-041-1426), space group (Pbnm), particle size 184 Å with phase fraction 75.1% and Na_{0.33}V₂O₅ (ICDD No. 01-073-6271), space group (C12/m1), particle size 992 Å with phase fraction 24.9% were observed in 5NV. Moreover, XRD patterns of samples 15NV and 25NV showed two crystalline phases of Na_{0.33}V₂O₅ (ICDD No. 01-073-6271), and NaV₃O₈ (ICDD No. 00-035-0436). The phase fraction of Na_{0.33}V₂O₅ increased from 24.9% to 95.2% with increasing *x* from 5 to 15, then it decreased to 17.6% with *x* going from 15 to 25 mol%. The phase fraction of NaV₃O₈ increased from 4.8% to 82.4% with *x* going from 15 to 25 mol%.

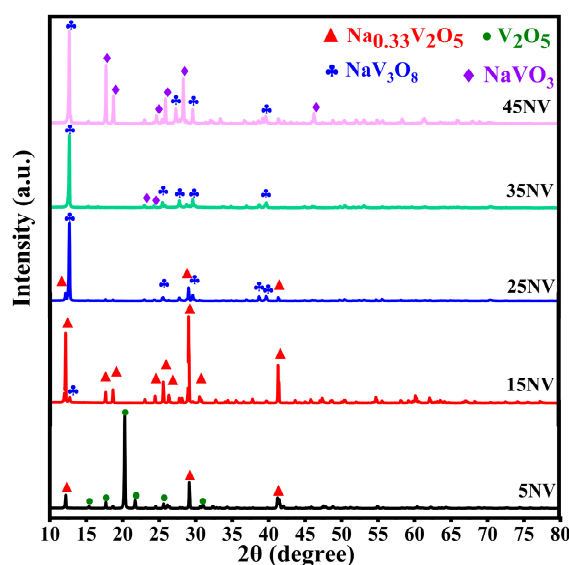


Figure 1. XRD patterns of *x*NV with '*x*' of 5, 15, 25, 35, and 45 mol%.

Table 1. The crystalline phases, lattice parameters, unit cell volume (V), full width at half maximum (FWHM), the interplanar lattice spacing (d), particle size, space group, and phase fraction of x NV ceramics.

x NN	Crystalline Phase	Lattice Parameters						V (\AA^3)	FWHM (deg.)	d (\AA)	Particle Size (\AA)	Space Group	Phase Fraction (%)
		a	b (\AA)	c	A	β (Degree)	γ						
5	V_2O_5	4.373	11.516	3.655	90	90	90	184 (2)	0.572 (8)	4.198 (5)	184 (22)	Pbnm	75.1
	β - $Na_{0.33}V_2O_5$	15.439	3.615	10.068	90	109.550	90	534 (4)	0.0977 (13)	7.256 (3)	992 (42)	C12/m1	24.9
15	β - $Na_{0.33}V_2O_5$	15.425	3.609	10.067	90	109.550	90	531 (49)	0.077 (3)	7.286 (5)	984 (64)	C12/m1	95.2
	NaV_3O_8	7.373	3.617	12.172	90	106.910	90	312 (53)	0.116 (9)	6.964 (2)	719 (2)	P121/m1	4.8
25	β - $Na_{0.33}V_2O_5$	15.424	3.609	10.066	90	109.550	90	529 (44)	0.100 (5)	7.264 (4)	834 (44)	C12/m1	17.6
	NaV_3O_8	7.315	3.608	12.160	90	107.750	90	309 (13)	0.104 (18)	6.970 (7)	796 (28)	P121/m1	82.4
35	NaV_3O_8	7.339	3.611	12.152	90	107.368	90	313 (27)	0.084 (2)	6.991 (8)	997 (27)	P121/m1	93.8
	α - $NaVO_3$	10.326	9.467	5.874	90	104.200	90	593 (56)	0.144 (14)	3.105 (11)	593 (56)	I12/a1	6.2
45	NaV_3O_8	7.349	3.615	12.168	90	107.368	90	315 (25)	0.092 (3)	6.982 (9)	905 (26)	P121/m1	38.1
	α - $NaVO_3$	10.551	9.484	5.876	90	104.210	90	571 (81)	0.150 (2)	3.104 (10)	582 (67)	I12/a1	61.9

In XRD patterns of 35NV were observed NaV_3O_8 (ICDD No. 00-035-0436), particle size 997 \AA with phase fraction (93.8%), and $NaVO_3$ (ICDD No. 01-070-1015) crystalline phase, particle size 593 \AA with space group (I12/a1), and phase fraction (6.2%). NaV_3O_8 and $NaVO_3$ crystalline phases were also observed in the XRD patterns of 45NV, but the phase fraction of NaV_3O_8 decreased to 38.1%, and that of $NaVO_3$ increased to 61.9%. As x increased, the major crystalline phase changed from V_2O_5 to $Na_{0.33}V_2O_5$ and later from NaV_3O_8 to $NaVO_3$.

It is noted that a slow quenching rate ($10\text{ }^\circ\text{C min}^{-1}$) formed the crystalline phases observed by XRD of x NV. This process allows the deposition of some crystalline phases in the matrix of samples to produce the ceramic phase, which was also influenced by the ambient atmosphere. Also, the crystalline phases formed, such as V_2O_5 , NaV_3O_8 , converted to $Na_{0.33}V_2O_5$ and $NaVO_3$; these structures mainly consisted of layers of VO_4 and VO_5 units, which is suitable for charge transfer processes in the Na-ion battery [25]. Since vanadium has multi-valance states, the transition between these phases appears as a reduction from V^{5+} to V^{4+} , facilitating polaron hopping and improving the conductivity of the ceramics samples [29].

Specifically, the crystalline phases known as NaV_3O_8 and $Na_{0.33}V_2O_5$ are referred to as vanadium bronze due to their characteristic layered structure, which enhances the process of Na^+ ion insertion and desertion [29,30]; therefore, x NV ceramics series have high electrical conductivity [31]. Table 1 shows the crystalline phases and their lattice parameters in x NV ceramics.

3.2. Morphological Features of 15NV

The morphology of ceramics 15NV observed by STEM is shown in Figure 2a, confirming the presence of nano-crystallites. Figure 2b–f shows STEM images of each component in 15NV and the EDS mapping.

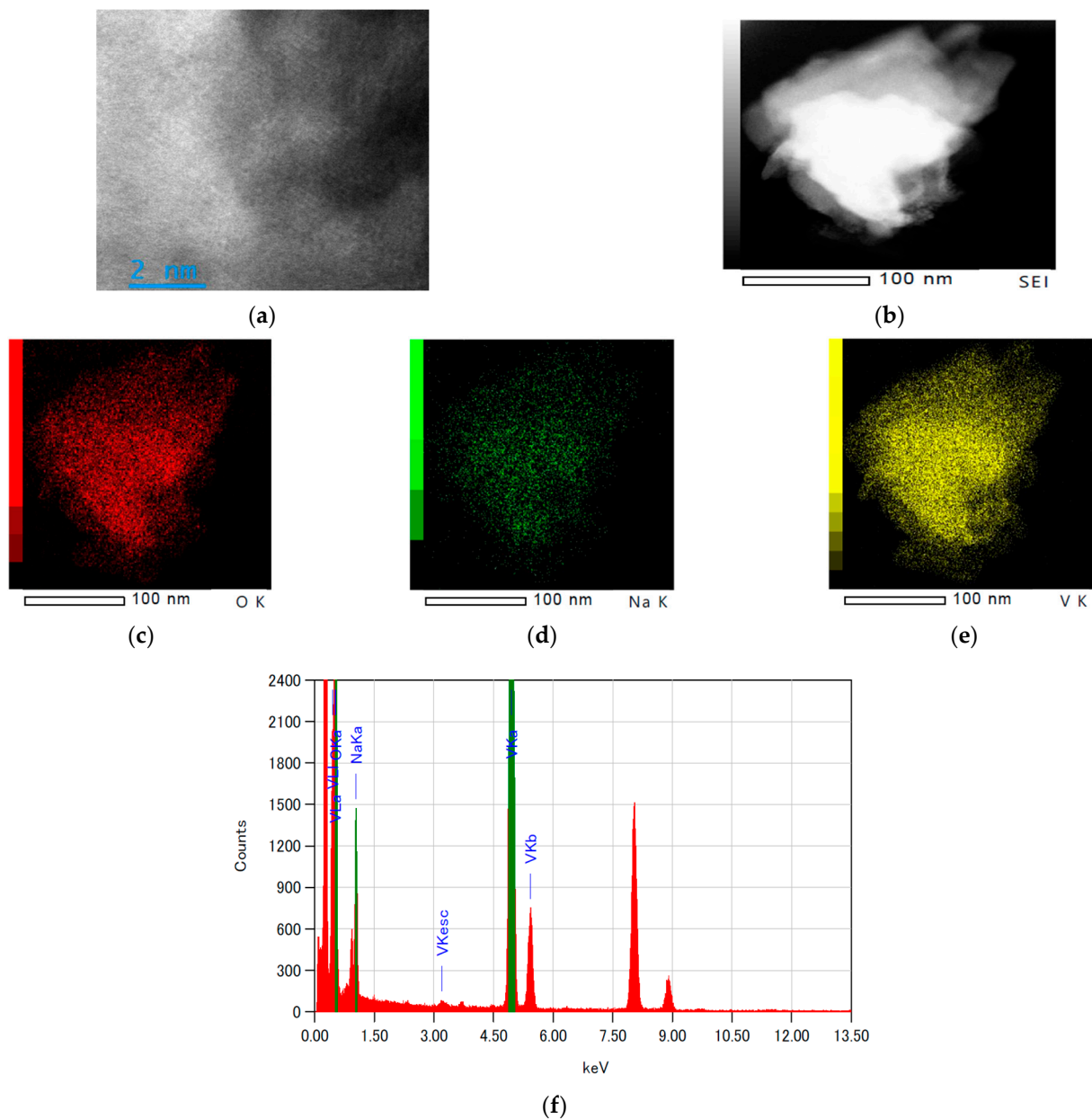


Figure 2. (a) STEM images of 15NV ceramic, (b) secondary electron images (SEI) in a scanning electron microscope HAADF-STEM image, EDS elemental mappings of Na (c), V (d), O (e), and EDS mappings with the overlap of other elements (f).

It is observed that the EDS analysis of this sample proved the existence of vanadium, sodium, and oxygen with a distribution of the mass ratios of O abundance lower than the theoretical value, and Na and V ratios are larger than those expected for $\text{Na}_{0.33}\text{V}_2\text{O}_5$, as shown in Table 2.

Table 2. Mass percentage of Na, V, and O atoms in 15NV compared with the theoretical percentage values of Na, V, and O in $\text{Na}_{0.33}\text{V}_2\text{O}_5$.

Element	Mass Ratio of Atoms (%)	Theoretical Value (%) ($\text{Na}_{0.33}\text{V}_2\text{O}_5$)
Na	5.79	4.00
V	64.08	53.80
O	30.13	42.20

3.3. FTIR Spectra of x NV

Figure 3 and Table 3 show the FTIR transmission spectra and peak assignments of x NV, respectively, with increasing Na_2O content. The transmission peak at 471 cm^{-1} in x NV is attributed to bending modes of the V_2O_5 network consisting of $[\text{VO}_5]$ polyhedra [32,33], and the peak intensity decreased as the Na_2O content increased. The transmission peak at 585 cm^{-1} for x NV can be assigned to the V-O-V symmetric stretching vibration [32,33]. The peak center was shifted to a lower wavenumber from 585 cm^{-1} to 557 cm^{-1} , when ' x ' increased from 5 to 45.

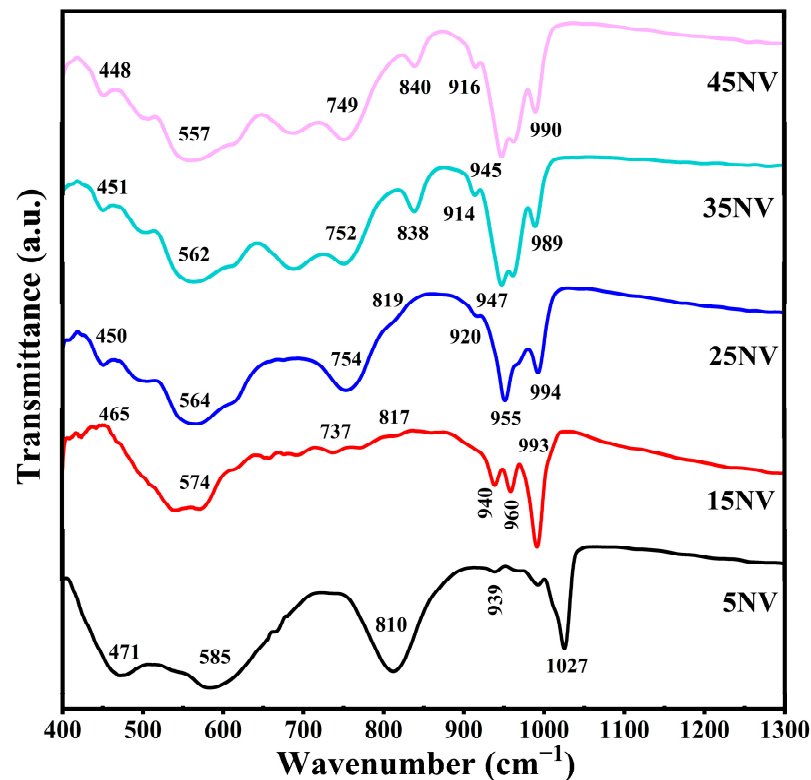


Figure 3. FTIR spectra of x NV with ' x ' of 5, 15, 25, 35, and 45 mol%.

Table 3. Peak assignments of FT-IR spectra for x NV with ' x ' of 5, 15, 25, 35, and 45 mol.%. The peak positions are given in cm^{-1} .

Peaks	5NV	15NV	25NV	35NV	45NV	Peak Assignment
1	471	465	450	451	448	Bending modes of the V_2O_5 network consisting of $[\text{VO}_5]$ polyhedra
2	585	574	564	562	557	V-O-V symmetric stretching vibrations
3	-	737	754	752	749	V-O-V asymmetric stretching vibrations
4	810	817	819	838	840	V-O-V deformation modes
5	939	940	920	914	916	Stretching vibration of distorted octahedra (VO_6)
6	-	960	955	947	945	V=O stretching vibration
7	1027	993	994	989	990	V=O stretching vibration of distorted square pyramids

The transmission peak at 737 cm^{-1} for x NV is ascribed to the asymmetric stretching vibration of $\text{V}(\text{T}_d)\text{O}_4$ [33–35]. The center of this peak was shifted to a higher wavenumber at 749 cm^{-1} for x NV as a function of the Na_2O content. The small transmission peak observed at 810 cm^{-1} is attributed to V-O-V deformation modes [32,33].

The strong transmission peak at 960 cm^{-1} is assigned to the V=O stretching vibration mode of the VO_5 pyramid [33,35,36], which is sensitive to intercalation and suggests that Na^+ ions are inserted between the V_2O_5 layers [36]. It is noted that a split of this peak is observed from FT-IR spectra of the x NV ceramics with ' x ' from 15 to 45. The splitting peak

at 939 cm^{-1} observed for the spectra of 5NV is attributed to V=O stretching of distorted octahedra, the peak center was shifted to 916 cm^{-1} , with 'x' increased from 5 to 45.

The peak observed at 1027 cm^{-1} is ascribed to V=O stretching of distorted square pyramids [33,37]. The peak intensities decreased and shifted to a lower wavenumber with Na_2O content. This result confirms the formation of the crystalline phase of a vanadium bronze $\text{Na}_{0.33}\text{V}_2\text{O}_5$ composed of VO_6 octahedra and VO_5 square pyramids as observed in XRD patterns (see Figure 1).

3.4. XAS of $x\text{NV}$

As shown in Figure 4a, the spectra of V K-edge XANES of $x\text{NV}$ ceramics were measured to identify the oxidation states of the vanadium. The pre-edge peak represents the transition from 1 s to 3 d orbital [38]. This is because the 3 d orbital of vanadium and the 2p orbital of oxygen form a hybrid orbital, a permitted transition in the case of non-octahedral symmetry [31,38]. Therefore, the pre-edge peak intensity depends on the coordination symmetry [33,38]. The peak intensities of samples 25NV, 35NV, and 45NV were higher than those of 15NV and 5NV.

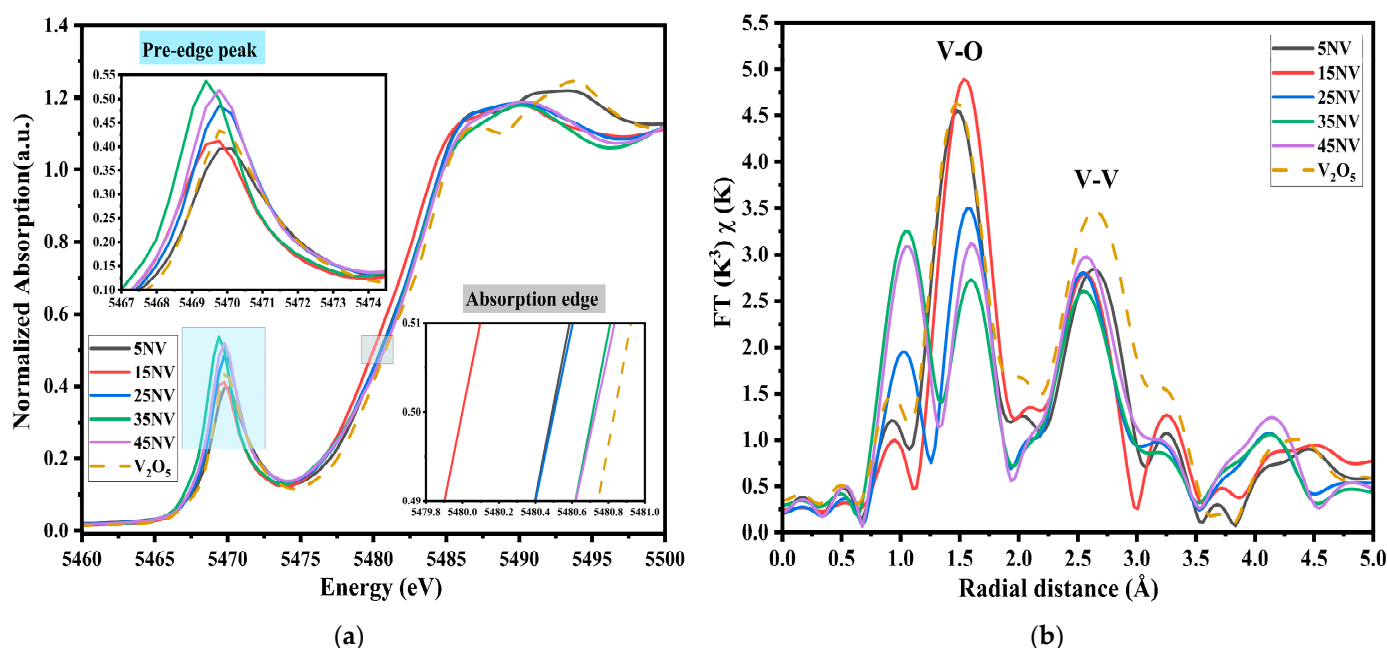


Figure 4. (a) V K-edge XANES and (b) V K-edge EXAFS (FT-EXAFS) spectra of V_2O_5 (yellow line) and $x\text{NV}$ with 'x' of 5, 15, 25, 35, and 45.

The lowest absorption edge for 15NV was observed at 5479 eV, while the absorption edge energy of 5NV, 25NV, 35NV, and 45NV ceramics was approximately at 5481 eV. Since the absorption edge energy increased, it implies an increasing oxidation state [3]. This shift to the lower energy side of 15NV is due to the formation of vanadium bronze. It is considered that the oxidation number of vanadium is reduced to maintain charge neutrality during the formation of vanadium bronze. Accordingly, a part of vanadium ions is reduced from V^{5+} to V^{4+} .

The Fourier transform of V K-edge EXAFS spectra of $x\text{NV}$ and V_2O_5 are shown in Figure 4b. The two peaks at 1.5 Å and 2.6 Å are associated with the V-O and V-V distances, respectively [39]. The position of the first peak for the 5NV ceramics is identical to that of V_2O_5 ; this is consistent with observing V_2O_5 peaks in the XRD results of 5NV. As x increases, the peak at 1.5 Å is shifted to the long-distance side, and the peak intensity decreases except for the 15NV ceramics. In comparison, the peak at 2.6 Å is moved toward the short-distance side, and the peak intensity decreases except for 45NV. The decrease in peak intensity is

due to increased vanadium site strain and reduced coordination number [40]. This result agrees with the result obtained by the pre-edge peak intensity analysis and XRD.

3.5. Electrical Properties of x NV

Electrical conductivity measurements were conducted over a wide range of frequencies and temperatures to determine the conductivity of x NV. Figure 5a shows the conductivity spectra for a ceramic containing 35 mol% Na_2O and is representative of the conductivity spectra for all the studied samples. The overall spectral features of this figure are observed as follows: (i) a frequency-independent conductivity, or DC conductivity, that is observed at all measured temperatures and dominates the spectra, (ii) frequency-dependent conductivity, or conductivity dispersion, which is present at higher frequencies and temperatures up to 10 °C, before disappearing from the measured frequency window. The obtained long DC conductivity plateaus are typical for fast electronic transport and are in line with the small polaron hopping mechanism between $\text{V}^{5+}/\text{V}^{4+}$ metal centers.

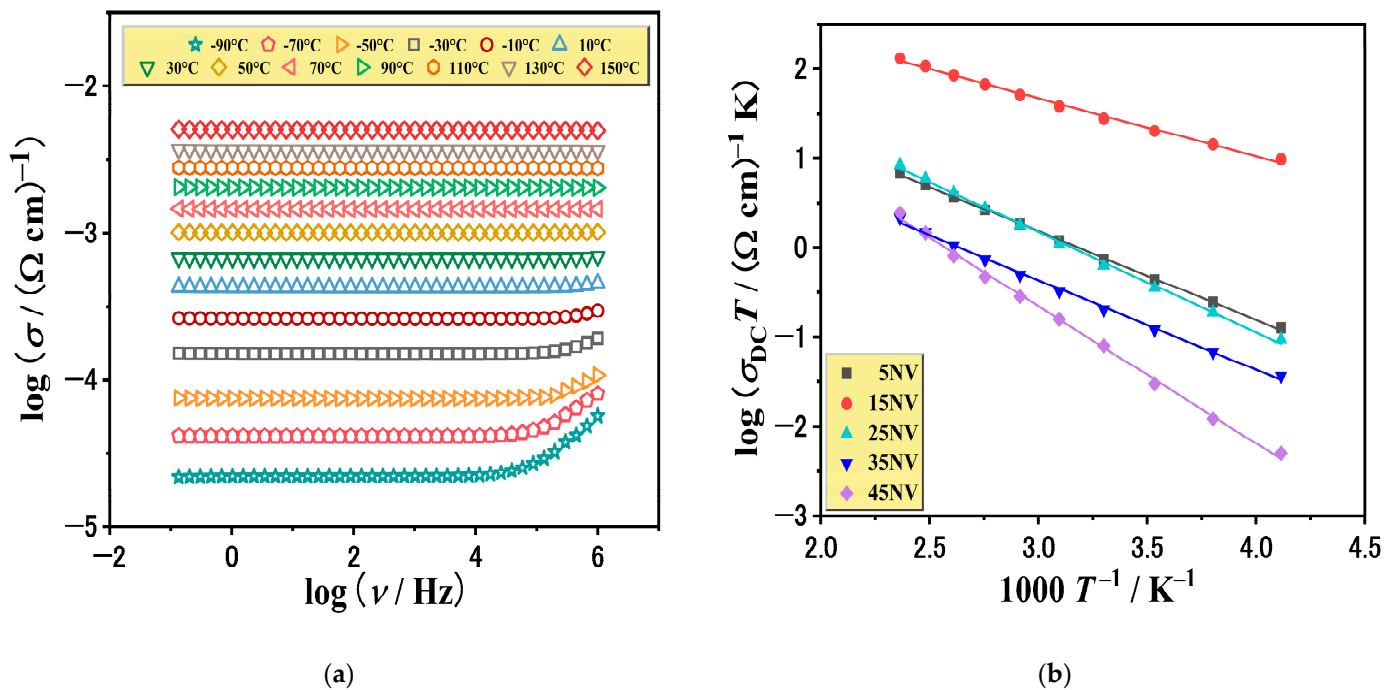


Figure 5. (a) Conductivity spectra of 35NV ceramics and (b) Arrhenius plot of DC conductivity of the x NV ceramics. Solid lines represent the least-square linear fits to experimental data.

The DC conductivity exhibits Arrhenius temperature dependence for all samples and has characteristic activation energy (see Figure 5b). The activation energy for the DC conductivity, E_{DC} , was determined for individual samples from the slope of $\log(\sigma_{DC} T)$ vs. $1000/T$ plot using the equation:

$$\sigma_{DC} T = \sigma_0^* \exp\left(\frac{-E_{DC}}{k_B T}\right) \quad (1)$$

where σ_{DC} is the DC conductivity, σ_0^* is the pre-exponent, k_B is the Boltzmann constant, and T is the temperature (K) [41–43]. The activation energy, E_{DC} , and DC conductivity, σ_{DC} , at 30 °C for all investigated samples are presented in Figure 6 and listed in Table 4. With increasing Na_2O content, the DC conductivity of x NV nonlinearly changes, with the maximum value of $0.0924 (\Omega \text{ cm})^{-1}$ obtained for the 15NV glass ceramics. The activation energy for DC conductivity, E_{DC} , follows the opposite trend with values increasing from 0.197 to 0.305 eV. Based on the E_{DC} values and features in conductivity spectra (Figure 5a), we can indicate that the dominant conduction mechanism is electronically governed by

small polaron hopping. However, the possible ionic contribution, along with contribution from various crystalline phases and microstructure, of prepared ceramics has also impact on the overall transport mechanism and conductivity trend and should be taken into account.

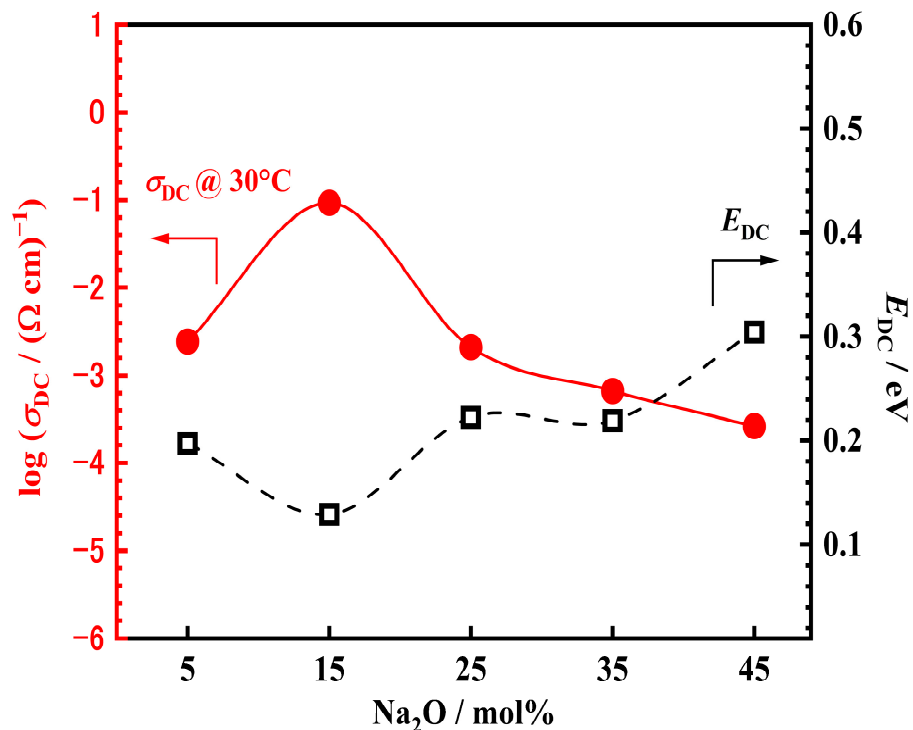


Figure 6. DC conductivity at 30 °C and activation energy for DC conductivity of x NV with ' x ' of $x = 5, 15, 25, 35,$ and 45 mol%. The lines are drawn as guides to the eye.

Table 4. DC conductivity, σ_{DC} , determined as a plateau value in the conductivity isotherms, activation energy, E_{DC} , for x NV with ' x ' of $x = 5, 15, 25, 35,$ and 45 mol%.

Ceramics Sample	σ_{DC} ((Ωcm) ⁻¹) *	E_{DC} (eV)
5NV	0.0024	0.197
15NV	0.0925	0.129
25NV	0.0021	0.223
35NV	6.67×10^{-4}	0.216
45NV	2.65×10^{-4}	0.305

* at 30 °C.

As previously mentioned, the presence of vanadium bronze in the system is highly favorable in the studied ceramics due to the high conductivity values of the vanadium bronze itself and its characteristic layered structure. PXRD measurements and analysis showed that the largest amount of vanadium bronze, $\text{Na}_{0.33}\text{V}_2\text{O}_5$, (95.2%) and NaV_3O_8 (4.8%) is present in sample 15NV. This feature can explain the deviation in linearity change in DC conductivity with composition and resulting maximum in DC conductivity for this sample. Such crystalline phases due to the characteristic layered structure have a positive effect on the process of Na^+ ion insertion and desertion [29,30] and are of great interest for target application as cathode material for secondary batteries.

3.6. Electrochemical Properties of x NV

Figure 7 shows the charge–discharge voltage curves of x NV ceramics in the voltage range from 0.8 to 3.6 V. The initial discharge capacities of 5NV, 15NV, 25NV, 35NV, and 45NV ceramics were 141, 203, 157, 118, and 101 mAh g^{-1} , respectively. The discharge

capacity decreased after 30 cycles, and the values became 45.3, 101.5, 102.0, 83.7, and 66.7 mAh g⁻¹ for 5NV, 15NV, 25NV, 35NV, and 45NV ceramics, respectively.

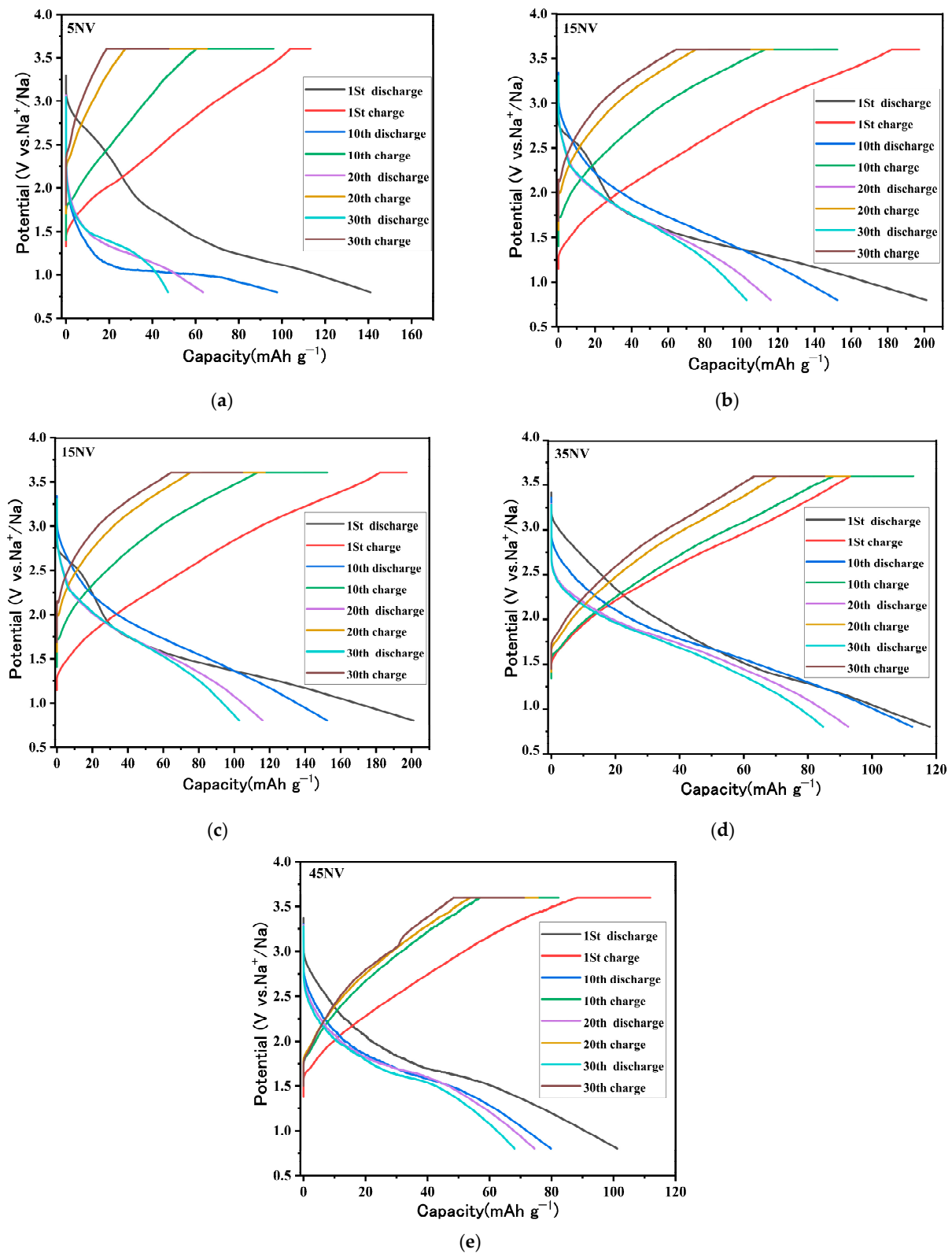


Figure 7. Charge–discharge curves of (a) 5NV, (b) 15NV, (c) 25NV, (d) 35NV and (e) 45NV.

Also, the charge–discharge voltage curves of the x NV ceramics sample appear without any specific plateau during the first cycle. The initial discharge capacity and capacity retention of x NV ceramics are summarized in Table 5.

Table 5. The capacity and capacity retention of x NV at a current rate of 50 mA g^{-1} in voltage range $0.8\text{--}3.6 \text{ V}$.

Ceramics Sample	Initial Discharge Capacity (mAh g^{-1})	Capacity Retention (%)
5NV	141	32.2
15NV	203	50.1
25NV	157	65.1
35NV	118	71.2
45NV	101	66.3

In Figure 8a, the discharge capacity of x NV was demonstrated during the first 30 cycles. The capacity retentions of the 5NV, 15NV, 25NV, 35NV, and 45NV ceramics after 30 cycles were 32.2, 50.1, 65.1, 71.2, and 66.3%, respectively.

The cathode active performances in the Na-ion battery of 15NV ceramic was measured under different voltage ranges under a current rate of 50 mA g^{-1} , as shown in Figure 8b. The capacity retention after 30 cycles significantly increased to 74% after being measured in a small voltage range between 1.5 and 4.0 V and up to 90% between 1.8 and 4.0 V while the initial capacity decreased to 82 mAh g^{-1} and 56 mAh g^{-1} , respectively. The slight decrease in the capacity is attributed to a small voltage range. Moreover, the capacities of 15NV sample under different current rates 5, 25, 50, 100, and 200 mA g^{-1} for 30 cycles were measured as shown in Figure 8c. The discharge capacity decreased with an increasing current rate, and the capacity retention after 30 cycles was 83.3%. It was noticed that the 15NV ceramics is stable under 100 mA g^{-1} , but after increasing the current rate to 200 mA g^{-1} , the capacity suddenly decreased to 1 mAh g^{-1} . Compared with the XRD patterns of the 15NV ceramics before battery measurement (Figure 1), the peaks of the NaV_3O_8 crystalline phase disappeared, and a new peak of NaVO_3 was confirmed after 10 cycles, with a unit cell volume of 558 \AA^3 , particle size 149 \AA and space group $I12/a1$, as shown in Figure 8d and Table 6. The phase fraction percentage of NaVO_3 increased from 76.26 to 80.2% and particle size slightly increased from 149 to 173 \AA with increasing cycles number from 10 to 30. In addition, the phase fraction percentage of $\text{Na}_{0.33}\text{V}_2\text{O}_5$ before charge and discharge and after 30 cycles decreased from 95.2 to 9.1%. Also, the particle size rapidly decreased from 984 \AA to 212 \AA with increasing cycles number from 1 to 30. The rapid decrease in the capacity is caused by the decrease in particle size, together with a reduction in the phase fraction percentage of $\text{Na}_{0.33}\text{V}_2\text{O}_5$ [43–47]. The decrease in the phase fraction of the $\text{Na}_{0.33}\text{V}_2\text{O}_5$ crystalline phase affects the discharge capacity and cyclability, as shown in Figure 8a. Moreover, a new line appeared at $2\Theta = 11.36^\circ$ after 20 cycles, ascribed to $\text{Na}_{0.287}\text{V}_2\text{O}_5$ crystalline phases with space group $(C12/c1)$, and phase fraction 6.07%. After 30 cycles, the phase fraction slightly increased to 10.68%. Figure 8d displays the XRD pattern of a cathode containing a 15NV sample after 30 cycles of the charge–discharge test. The considerable noise compared to other XRD patterns may be due to the mixing of acetylene black or PTFE with the cathode material [44–48].

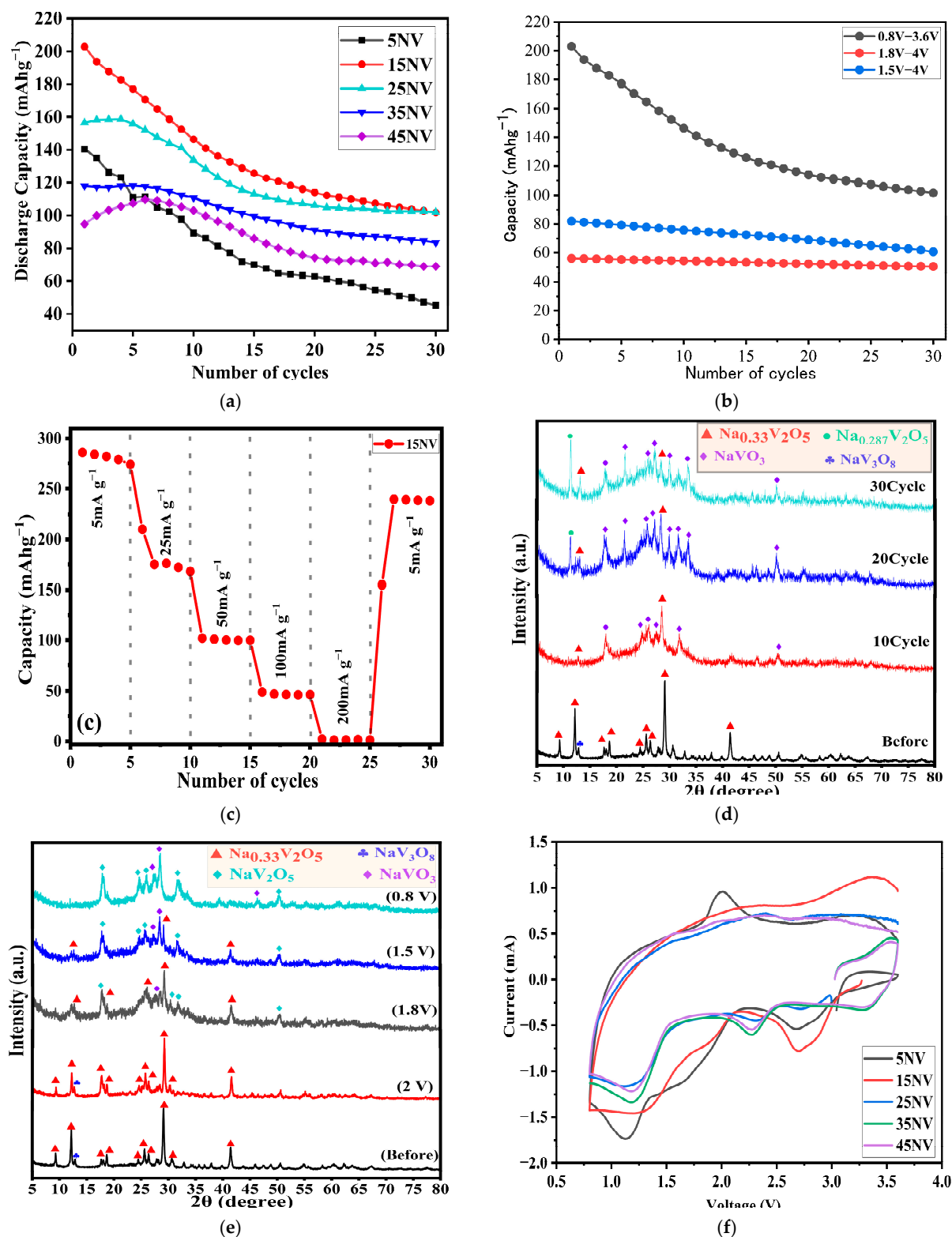


Figure 8. (a) The cyclability of x NV after 30 cycles, (b) the cyclability of 15NV under different voltage ranges, (c) the cyclability of 15NV ceramics under different current rates, (d) XRD pattern of 15NV before and after 10, 20, and 30 times charge–discharge cycles, (e) XRD pattern of 15NV ceramics before and after charging the SIB battery at 2.0, 1.8, 1.5, and 0.8 V. (f) The cyclic voltammetry (CV) curves of x NV ceramics with ‘ x ’ of 5, 15, 25, 35, and 45.

Table 6. The crystalline phases, lattice parameters, unit cell volume (V), full width at half maximum (FWHM), the interplanar lattice spacing (d), particle size, space group, and phase fraction of 15NV before and after 10, 20, and 30 cycles.

Cycles	Crystalline Phase	Lattice Parameters						V (Å ³)	FWHM (deg.)	d (Å)	Particle Size (Å)	Space Group	Phase Fraction (%)
		a	b (Å)	c	α	β	γ						
before	β -Na _{0.33} V ₂ O ₅	15.425	3.609	10.067	90	109.550	90	531 (49)	0.077 (3)	7.286 (5)	984 (64)	C12/m1	95.2
	NaV ₃ O ₈	7.373	3.617	12.172	90	106.910	90	312 (53)	0.116 (9)	6.964 (2)	719 (27)	P121/m1	4.8
10	α -NaVO ₃	10.492	9.432	5.862	90	108.800	90	558 (22)	0.572 (8)	3.225 (5)	149 (24)	C12/c1	76.26
	β -Na _{0.33} V ₂ O ₅	14.883	3.602	9.884	90	109.900	90	502 (16)	0.360 (2)	7.124 (2)	235 (16)	C12/m1	23.74
20	α -NaVO ₃	10.335	9.475	5.881	90	104.200	90	512 (47)	0.440 (11)	3.442 (9)	193 (47)	I12/a1	78.35
	Na _{0.287} V ₂ O ₅	10.096	3.615	10.096	90	109.549	90	388 (30)	0.210 (16)	7.756 (3)	398 (31)	C12/m1	6.07
	β -Na _{0.33} V ₂ O ₅	15.028	3.636	9.979	90	109.900	90	528 (35)	0.350 (5)	7.272 (3)	244 (35)	C12/m1	15.58
30	α -NaVO ₃	10.563	9.474	5.883	90	108.430	90	568 (21)	0.394 (13)	3.452 (7)	173 (42)	C12/c1	80.20
	Na _{0.287} V ₂ O ₅	10.116	3.622	10.484	90	109.610	90	420 (38)	0.199 (18)	7.806 (10)	420 (38)	C12/m1	10.68
	β -Na _{0.33} V ₂ O ₅	14.370	3.563	9.626	90	109.980	90	505 (35)	0.372 (5)	7.292 (3)	212 (36)	C12/m1	9.12

For the sample of 5NV, including crystalline phases attributed to V₂O₅, the initial discharge capacity was relatively high at 141 mAh g⁻¹, and the capacity retention after 30 cycles was the lowest at 32.2%. From xNV battery measurement and XRD results, one can conclude that forming vanadium bronze, such as Na_{0.33}V₂O₅ and NaV₃O₈, is indispensable for improving capacity retention [43,44].

Table 7 summarizes the results of Na-ion batteries containing sodium vanadate, sodium manganese oxide, and sodium cobalt oxide as the cathode material. However, it should be noted that each measurement condition is different. The highest capacity of 145.8 mAh g⁻¹ with NaV₃O₈ nanowires as the positive electrode was recorded under a current density of 10 mA g⁻¹ [49]. As a result of battery performance measurement using Na_{0.44}MnO₂ [10] or Na_{0.71}MnO₂ [50], which contain manganese as a transition metal, both having a layered structure, had cathode capacities of 128 and 75.2 mAh g⁻¹, respectively. These capacities were similar to or slightly lower than those of sodium vanadate.

Table 7. Comparison of the capacity of Na-ion batteries containing sodium vanadate or transition metal oxides.

Compound	Capacity [mAh g ⁻¹]	Capacity Retention Rate [%]/(cycle)	Current Density [mA g ⁻¹]	Voltage Range (V)	Ref.
NaV ₆ O ₁₅	157	73.8 (50)	20	1.5–3.8	[48]
Na _{0.282} V ₂ O ₅	130	91.5 (70)	1000	1.8–3.8	[49]
NaV ₃ O ₈	145.8	91.1 (50)	10	1.5–4.0	[51]
Na _{0.44} MnO ₂	128	97 (100)	100	2.0–4.0	[10]
Na _{0.71} CoO ₂	75.2	93 (100)	40	2.0–3.9	[50]
15NV	203	50.1 (30)	50	0.8–3.6	This work
15NV	82	78 (30)	50	1.5–4.0	This work
15NV	56	90 (30)	50	1.8–4.0	This work
35NV	118	71.2 (30)	50	0.8–3.6	This work

The initial discharge capacity of 203 mAh g⁻¹ obtained from 15NV ceramics was more significant than that of other cathode materials. However, as the cycle progresses, the peaks of the CV curve become broad, and the long-range order may deteriorate. In addition, the XRD pattern of the Na₂V₂O₅ crystalline phase obtained by this reversible change had a trend similar to that of the NaV₂O₅ crystalline phase. From the findings above, it can be observed that upon repetitive charging and discharging within the voltage range of 0.8 to 3.6 V, the Na_{0.33}V₂O₅ crystalline phase undergoes irreversible changes in its structure, a transformation into the NaV₂O₅ crystalline phase takes place, as shown in Figure 8e and Table 8. Then, 1 mol of Na ions is reversibly intercalated-deintercalated into 1 mol of NaV₂O₅ crystalline phase. NaV₂O₅ and NaV₃O₈ crystalline phases lose their crystallinity over the cycling process, reducing the battery performance. However, this crystallinity problem may be remedied by the annealing process. Hanna et al. reported that when NaV₃O₈ was heat-treated at 400 °C for three hours, the capacity retention after 50 cycles improved from 51.9% to 91.1% [51].

Table 8. The crystalline phases, lattice parameters, unit cell volume (*V*), full width at half maximum (FWHM), the interplanar lattice spacing (*d*), particle size, space group, and phase fraction of 15NV ceramics, before charging, and after charging at 2, 1.8, 1.5, and 0.8 V.

Voltage	Crystalline Phase	Lattice Parameters						<i>V</i> (Å ³)	FWHM (deg.)	<i>d</i> (Å)	Particle size (Å)	Space Group	Phase Fraction (%)
		<i>a</i>	<i>b</i> (Å)	<i>c</i>	<i>α</i>	(Degree) <i>β</i>	<i>γ</i>						
Before	β-Na _{0.33} V ₂ O ₅	15.425	3.609	10.067	90	109.550	90	531 (49)	0.077 (3)	7.286 (5)	984 (64)	C12/m1	95.2
	NaV ₃ O ₈	7.373	3.617	12.172	90	106.910	90	312 (53)	0.116 (9)	6.964 (2)	719 (27)	P121/m1	4.8
2 V	β-Na _{0.33} V ₂ O ₅	15.349	3.608	10.048	90	109.200	90	522 (16)	0.215 (9)	7.226 (5)	389 (16)	A12/m1	94.8
	NaV ₃ O ₈	7.361	3.642	12.165	90	106.840	90	329 (34)	0.250 (3)	6.958 (6)	329 (34)	P12/m1	5.2
1.8 V	NaVO ₃	10.542	9.456	5.872	90	108.430	90	567 (107)	0.282 (19)	3.052 (6)	304 (56)	C1/c1	4.6
	NaV ₂ O ₅	11.029	3.623	4.934	90	90	90	197 (30)	0.250 (8)	2.943 (3)	398 (30)	Pmmn	34.8
	β-Na _{0.33} V ₂ O ₅	15.406	3.614	10.109	90	109.411	90	528 (16)	1.100 (2)	7.660 (6)	177 (22)	P12/m1	60.6
1.5 V	NaVO ₃	10.338	9.478	5.883	90	104.200	90	559 (290)	0.080 (2)	3.064 (6)	1011 (165)	I12/a1	20.4
	NaV ₂ O ₅	11.489	3.615	4.869	90	90	90	202 (32)	0.280 (7)	2.843 (4)	320 (32)	P21mn	50.6
	β-Na _{0.33} V ₂ O ₅	15.288	3.701	10.153	90	109.900	90	515 (10)	1.3 (2)	7.09 (10)	67 (10)	C12/m1	29
0.8 V	NaVO ₃	10.507	9.446	5.870	90	108.800	90	545 (18)	0.57 (7)	3.435 (3)	148 (18)	C1/c1	31.9
	NaV ₂ O ₅	11.394	3.607	4.553	90	90	90	187 (60)	0.38 (10)	2.281 (6)	234 (47)	Pmmn	68.1

The capacity gradually decreased, as reported by Köhler et al. [52], namely, the XRD patterns of LiV₃O₈ after 100 cycles showed decreased crystallinity compared to the case without cycling. This means that there is a slight decrease in the crystallinity of NaV₃O₈ throughout the cycle, and the reduction in the ability to insert Na ions led to the deterioration of battery performance. In addition, an irreversible release of VO²⁺ ions was confirmed in Li_xV₂O₅ (*x* > 1) [53]. Huinan et al. proposed that V₂O₅ irreversibly transforms into NaV₂O₅ by the insertion of Na ions, and then the following reaction occurs reversibly [46].



Figure 8f shows the cyclic voltammetry (CV) curves of *x*NV ceramics. Before the charge–discharge test, the CV curves were measured with a battery using *x*NV as the

cathode material. Figure 8f shows two reduction peaks of 5NV ceramics observed at 1.13 and 2.68 V, and one oxidation peak can be observed at 2.01 V. The reduction peaks of 15NV were located at 1.12, 1.78, and 2.69 V, while the oxidation peak showed only at 2.36 V. The reduction peaks of 25NV ceramics were observed at 0.89, 2.31, and 2.69 V; the oxidation peaks were observed at 2.38 and 2.83 V. The reduction peaks of 35NV were observed at 1.16, 2.28, and 3.26 V; the oxidation peaks were observed at 2.38 and 2.90 V. The reduction peaks of 45NV were observed at 1.18, 2.27, and 3.28 V; the oxidation peaks were observed at 2.39 and 2.92 V. The reduction peaks of the $\text{NaV}_6\text{O}_{15}$ phase are observed at 2.50 and 2.80 V [48].

The reduction peaks of 5NV, 15NV, and 25NV ceramics samples, except the peak of near 1 V, are related to the $\text{NaV}_6\text{O}_{15}$ crystalline phase, as shown in Table 8. Furthermore, the reduction peaks of the NaV_3O_8 crystalline phase are identified at 2.35, 2.36, and 2.69 V [54]. The reduction peaks at 2.27 and 3.28 V of 45NV ceramics are related to the NaV_3O_8 crystalline phase [54,55]. A reduction peak near 1 V was observed in all x NV ceramics samples, but a corresponding oxidation peak could not be observed. This result shows that an irreversible structural change occurs near 1 V using x NV ceramics samples as the cathode material.

For α - NaV_2O_5 , reduction and oxidation peaks were observed at 2.01 V and 2.30 V, respectively [45]. Therefore, this redox peak is considered to be derived from α - NaV_2O_5 . The slight shift in the peak position may be due to the difference between the inserted ions being Li [53] or Na (this work). This result reaffirms the peak assignment to NaV_2O_5 in the XRD pattern analysis results (Figure 8).

Figure 9a,b shows the Nyquist plots of x NV ceramics samples before and after the battery test obtained by electrochemical impedance spectra (EIS) measurements. A semicircle in the high-frequency region and a Warburg impedance in the low-frequency region is observed for the x NV system. The inserted figure in Figure 9a shows an equivalent circuit for the impedance spectra. The equivalent circuit mainly consists of the solution resistance (R_1), the resistance of SEI films (R_2), the charge transfer resistance (R_3), the constant phase element ($CPE1$, $CPE2$), and Warburg impedance (Z_w) [54–56]. The fitting results by the equivalent circuit are shown in Table 9. It is noted that the charge in R_1 and R_2 is very small for all the ceramics samples before and after the battery tests. The slight increase in R_2 may be attributed mainly to the continuous deposition of sodium ions in the solid electrolyte interphase film (SEI) [55,56]. On the other hand, R_3 increased significantly by the charging and discharging process. Especially the R_3 value of the 5NV sample after the 30th cycle ($R_3 = 241 \Omega$) is 8.92 times higher than that before the battery tests ($R_3 = 27 \Omega$), while in samples of 15NV, 25NV, 35NV, and 45NV, R_3 increased by a factor of 3.89, 3.57, 3.44, and 2.91, respectively.

Table 9. EIS measurement fitting results of x NV samples before and after 30 cycles of battery test by the equivalent circuit.

Sample	Before			After		
	R_1 (Ω)	R_2 (Ω)	R_3 (Ω)	R_1 (Ω)	R_2 (Ω)	R_3 (Ω)
5NV	17.2	34.5	27.0	22.5	34.6	241
15NV	29.8	30.2	50.3	11.7	15.3	196
25NV	15.2	12.5	43.3	30.5	34.9	155
35NV	17.7	17.0	34.8	14.1	10.0	120
45NV	15.7	19.4	50.8	21.6	12.4	148

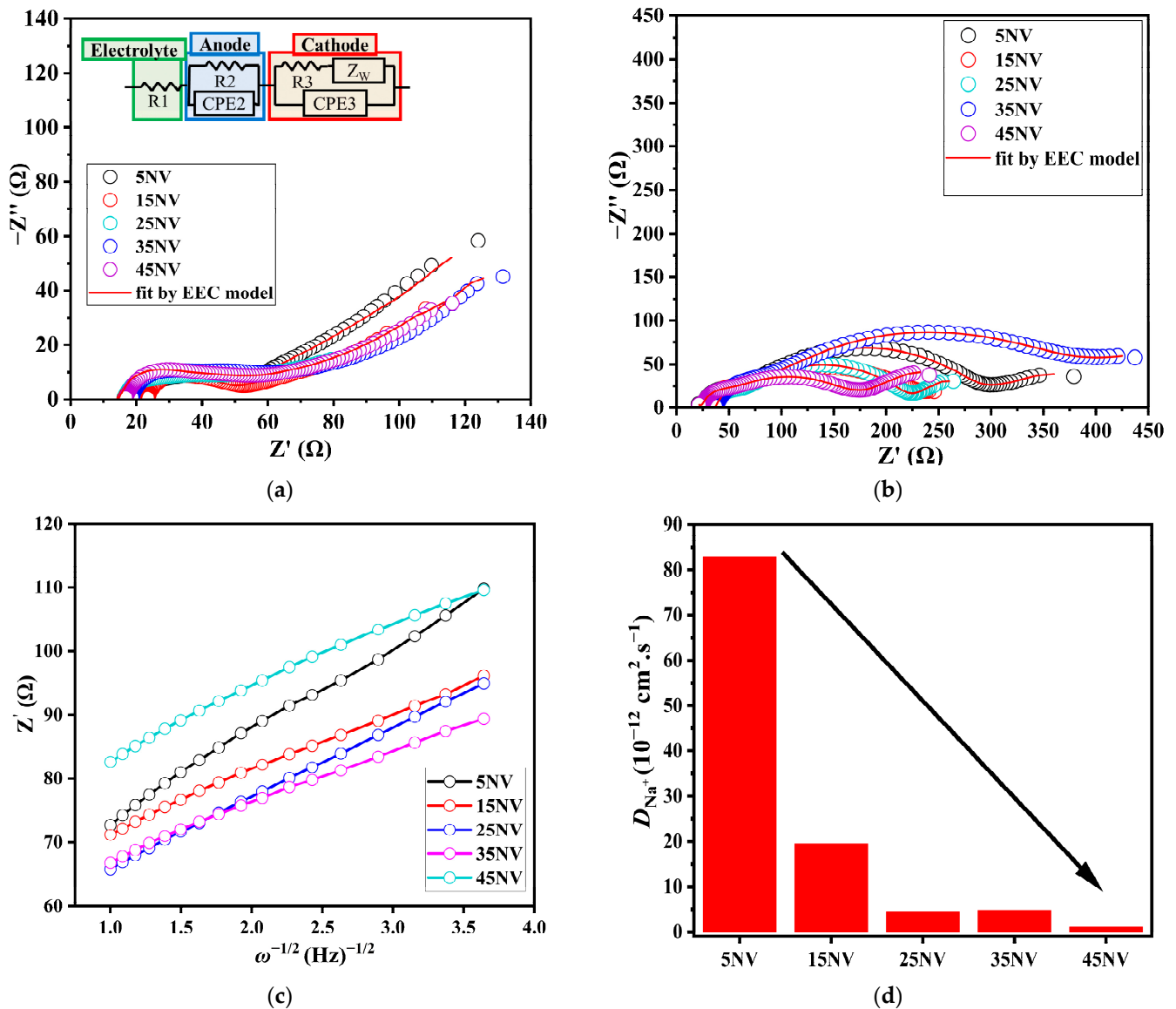


Figure 9. EIS measurement of xNV with 'x' of 5, 15, 25, 35, and 45 (a) before and (b) after the 30-cycle charge–discharge test, (c) the relationship between Z' and $\omega^{-1/2}$, and (d) the diffusion coefficient (D_{Na^+}) of xNV.

The battery performance deteriorated due to increased charge transfer resistance by repeating the charging and discharging process. The following two equations can be applied to calculate the diffusion coefficient (D_{Na^+}) of the sodium ions [53,55].

$$Z' = R1 + R2 + R3 + s\omega^{-1/2} \quad (3)$$

$$D_{Na^+} = 0.5R^2T^2/A^2n^4F^4C^2s^2 \quad (4)$$

In the equations, s is the Warburg factor, the slope of the line in Figure 9c. R is the gas constant, T is the temperature, A is the surface area, n is the number of reaction electrons, F is the Faraday constant, and C is the sodium ion concentration in the cathode. The Na^+ diffusion coefficient (D_{Na^+}) of xNV gradually decreased from 8.28×10^{-11} cm² s⁻¹ to 1.23×10^{-12} cm² s⁻¹ with increasing 'x' from 5 to 45 mol% Na₂O as shown in Figure 9d.

The EIS measurement correlates the charge-transfer resistance ($R3$) and D_{Na^+} . So, the low charge transfer resistance is advantageous to insert and deinsert sodium ions to/from

the cathode material. As mentioned above, the high ratio of $R3$ before and after the battery test for 30 cycles was recorded for 5NV and 15NV, caused by a decrease in insert and deinsert Na^+ ions of these samples gradually decreasing. This behavior is related to the destruction that occurred in the layer structure of $\text{Na}_{0.33}\text{V}_2\text{O}_5$ in 15NV, which was related to a decrease in the phase fraction of $\text{Na}_{0.33}\text{V}_2\text{O}_5$ from 95.2% to 9.1% after 30 cycles. In addition, the small $R3$ ratio for 35NV compared with 15NV, therefore the reduction in D_{Na^+} value for 35NV after 30 cycles, is related to the structure stability and high-capacity retention compared with 15NV. We conclude that 15NV shows a high initial capacity at 203 mAh g^{-1} , and 35NV ceramics have good capacity retention at 71.2%; therefore, they are promising cathode materials for SIBs.

4. Conclusions

XRD, XAS, CV, EIS, and charge–discharge capacity tests of the SIB containing $x\text{NV}$ ceramics samples as cathode materials were evaluated. A relationship between the local structure and electrochemical properties of $x\text{NV}$ with ‘ x ’ from 5 to 45 mol% was investigated. From the XRD results, V_2O_5 , $\text{Na}_{0.33}\text{V}_2\text{O}_5$, NaV_3O_8 , and NaVO_3 crystalline phases were observed in $x\text{NV}$. XANES study of $x\text{NV}$ showed that the absorption edge of 15NV ceramics is shifted towards the lowest energy side. This shift shows the reduction of V^{5+} to V^{4+} ions; therefore, V^{4+} is the most abundant in $\text{Na}_{0.33}\text{V}_2\text{O}_5$. The Fourier transform of EXAFS curves showed the micro-environment of vanadium; it is close to that in V_2O_5 . Furthermore, the V–O bond length in the first coordination sphere and the V–V length in the second coordination sphere increased and decreased, respectively, with x . In the EIS measurement, the charge transfer resistance increased from 50.3Ω to 196Ω during the charge–discharge capacity test in 15NV ceramics. The diffusion coefficient of sodium (D_{Na^+}) decreased from 8.28×10^{-11} to $1.23 \times 10^{-12} \text{ cm}^2 \text{ s}^{-1}$ with increasing ‘ x ’ from 5 to 45 mol% Na_2O . The CV measurement observed a reduction peak near 1.30 V, 1.80 V, and 2.70 V, while it did not show any oxidation peaks; therefore, an irreversible reaction occurred. In addition, precipitation of NaV_2O_5 was observed after the charge–discharge test. So it is considered that the irreversible reaction is a transformation from $\text{Na}_{0.33}\text{V}_2\text{O}_5$ to NaV_2O_5 . The highest discharge capacity of 203 mAh g^{-1} was recorded for the 15NV ceramics at the current rate of 50 mA g^{-1} . Finally, we can conclude that the precipitation of vanadium bronze is considered promising for achieving higher capacity for Na-ion batteries.

Author Contributions: Conceptualization, A.I. and S.K.; methodology, S.W.; software, A.I.; validation, A.I., S.K. and Z.H.; formal analysis, A.I.; investigation, A.I.; resources, S.K.; data curation, S.W.; writing—original draft preparation, A.I.; writing—review and editing, S.K., Z.H., M.Y.H., L.P., M.R. and E.K. visualization, A.I.; supervision, S.K.; project administration, S.K.; funding acquisition, S.K. All authors have read and agreed to the published version of the manuscript.

Funding: This research was funded by JSPS KAKENHI Grant Number 23H02070 and Tokyo Metropolitan Government Advanced Research, Grant No. H29-1.

Data Availability Statement: Not applicable.

Conflicts of Interest: The authors declare no conflict of interest.

References

1. Kim, T.; Song, W.; Son, D.-Y.; Ono, L.K.; Qi, Y. Lithium-ion batteries: Outlook on present, future, and hybridized technologies. *J. Mater. Chem. A* **2019**, *7*, 2942–2964. [[CrossRef](#)]
2. Li, S.; Dong, Y.; Xu, L.; Xu, X.; He, L.; Mai, L. Effect of carbon matrix dimensions on the electrochemical properties of $\text{Na}_3\text{V}_2(\text{PO}_4)_3$ nanograins for high-performance symmetric sodium-ion batteries. *Adv. Mater.* **2014**, *26*, 3545–3553. [[CrossRef](#)] [[PubMed](#)]
3. Dong, Y.; Xu, J.; Chen, M.; Guo, Y.; Zhou, G.; Li, N.; Zhou, S.; Wong, C.-P. Self-assembled $\text{NaV}_6\text{O}_{15}$ flower-like microstructures for high-capacity and long-life sodium-ion battery cathode. *Nano Energy* **2020**, *68*, 104357. [[CrossRef](#)]
4. Arroyo-de Dompablo, M.E.; Ponrouch, A.; Johansson, P.; Palacín, M.R. Achievements, challenges, and prospects of calcium batteries. *Chem. Rev.* **2020**, *120*, 6331–6357. [[CrossRef](#)]
5. Liu, Y.; Sun, Z.; Tan, K.; Denis, D.K.; Sun, J.; Liang, L.; Hou, L.; Yuan, C. Recent progress in flexible non-lithium based rechargeable batteries. *J. Mater. Chem. A* **2019**, *7*, 4353–4382. [[CrossRef](#)]

6. Aurbach, D.; Lu, Z.; Schechter, A.; Gofer, Y.; Gizbar, H.; Turgeman, R.; Cohen, Y.; Moshkovich, M.; Levi, E. Prototype systems for rechargeable magnesium batteries. *Nature* **2000**, *407*, 724–727. [[CrossRef](#)]
7. Kim, K.S.; Lee, S.; Ting, T.O.; Yang, X.-S. Atomic scheduling of appliance energy consumption in residential smart grids. *Energies* **2019**, *12*, 3666. [[CrossRef](#)]
8. Yabuuchi, N.; Kubota, K.; Dahbi, M.; Komaba, S. Research development on sodium-ion batteries. *Chem. Rev.* **2014**, *114*, 11636–11682. [[CrossRef](#)]
9. Jin, T.; Li, H.; Zhu, K.; Wang, P.-F.; Liu, P.; Jiao, L. Polyanion-type cathode materials for sodium-ion batteries. *Chem. Soc. Rev.* **2020**, *49*, 2342–2377. [[CrossRef](#)]
10. Slater, M.D.; Kim, D.; Lee, E.; Johnson, C.S. Sodium-ion batteries. *Adv. Funct. Mater.* **2013**, *23*, 947–958. [[CrossRef](#)]
11. Wei, T.; Tang, Z.; Yu, Q.; Chen, H. Smart antibacterial surfaces with switchable bacteria-killing and bacteria-releasing capabilities. *ACS Appl. Mater. Interfaces* **2017**, *9*, 37511–37523. [[CrossRef](#)] [[PubMed](#)]
12. Wang, T.; Su, D.; Shanmukaraj, D.; Rojo, T.; Armand, M.; Wang, G. Electrode materials for sodium-ion batteries: Considerations on crystal structures and sodium storage mechanisms. *Electrochem. Energy Rev.* **2018**, *1*, 200–237. [[CrossRef](#)]
13. Ibrahim, A.; Shiraishi, M.; Homonnay, Z.; Krehula, S.; Marciaus, M.; Bafti, A.; Pavić, L.; Kubuki, S. Photocatalytic and Cathode Active Abilities of Ni-Substituted α -FeOOH Nanoparticles. *Int. J. Mol. Sci.* **2023**, *24*, 14300. [[CrossRef](#)]
14. Yabuuchi, N.; Yoshida, H.; Komaba, S. Crystal structures and electrode performance of α -NaFeO₂ for rechargeable sodium batteries. *Electrochemistry* **2012**, *80*, 716–719. [[CrossRef](#)]
15. Sun, S.; Chen, Y.; Cheng, J.; Tian, Z.; Wang, C.; Wu, G.; Liu, C.; Wang, Y.; Guo, L. Constructing dimensional gradient structure of Na₃V₂(PO₄)₃/C@CNTs-WC by wolfram substitution for superior sodium storage. *Chem. Eng. J.* **2021**, *420*, 130453. [[CrossRef](#)]
16. Tepavcevic, S.; Xiong, H.; Stamenkovic, V.R.; Zuo, X.; Balasubramanian, M.; Prakapenka, V.B.; Johnson, C.S.; Rajh, T. Nanostructured bilayered vanadium oxide electrodes for rechargeable sodium-ion batteries. *ACS Nano* **2011**, *6*, 530–538. [[CrossRef](#)]
17. Raju, V.; Rains, J.; Gates, C.; Luo, W.; Wang, X.; Stickle, W.F.; Stucky, G.D.; Ji, X. Superior Cathode of Sodium-Ion Batteries: Orthorhombic V₂O₅ Nanoparticles Generated in Nanoporous Carbon by Ambient Hydrolysis Deposition. *Nano Lett.* **2014**, *14*, 4119–4124. [[CrossRef](#)]
18. Yuan, S.; Liu, Y.-B.; Xu, D.; Ma, D.-L.; Wang, S.; Yang, X.-H.; Cao, Z.-Y.; Zhang, X.-B. Pure Single-Crystalline Na_{1.1}V₃O_{7.9} Nanobelts as Superior Cathode Materials for Rechargeable Sodium-Ion Batteries. *Adv. Sci.* **2015**, *2*, 1400018. [[CrossRef](#)]
19. Liu, H.; Wang, Y.; Li, L.; Wang, K.; Hosono, V.; Zhou, V. Facile synthesis of NaV₆O₁₅ nanorods and its electrochemical behavior as cathode material in rechargeable lithium batteries. *J. Mater. Chem.* **2009**, *19*, 7885–7891. [[CrossRef](#)]
20. Bach, S.; Baffier, N.; Pereira-Ramos, J.P.; Messina, R. Electrochemical sodium intercalation in Na_{0.33}V₂O₅ bronze synthesized by a sol-gel process. *Solid State Ionics* **1989**, *37*, 41–49. [[CrossRef](#)]
21. Liu, H.; Zhou, H.; Chen, L.; Tang, Z.; Yang, W. Electrochemical insertion/deinsertion of sodium on NaV₆O₁₅ nanorods as cathode material of rechargeable sodium-based batteries. *J. Power Sources* **2011**, *196*, 814–819. [[CrossRef](#)]
22. Liu, J.; Tang, S.; Lu, Y.; Cai, G.; Liang, S.; Wang, W.; Chen, X. Synthesis of Mo₂N nanolayer coated MoO₂ hollow nanostructures as high-performance anode materials for lithium-ion batteries. *Energy Environ. Sci.* **2013**, *6*, 2691–2697. [[CrossRef](#)]
23. Liu, J.; Lu, P.-J.; Liang, S.; Liu, J.; Wang, W.; Lei, M.; Tang, S.; Yang, Q. Ultrathin Li₃VO₄ nanoribbon/graphene sandwich-like nanostructures with ultrahigh lithium ion storage properties. *Nano Energy* **2015**, *12*, 709–724. [[CrossRef](#)]
24. Yamada, H.; Ueda, Y. Magnetic, electric and structural properties of β -A_xV₂O₅ (A = Na, Ag). *J. Phys. Soc. Jpn.* **1999**, *68*, 2735–2740. [[CrossRef](#)]
25. Qin, M.-L.; Liu, W.-M.; Xiang, Y.-J.; Wang, W.-G.; Shen, B. Synthesis and electrochemical performance of V₂O₅/NaV₆O₁₅ nanocomposites as cathode materials for sodium-ion batteries. *Trans. Nonferrous Met. Soc. China* **2020**, *30*, 2200–2206. [[CrossRef](#)]
26. Kawada, K.; Yamashita, K.; Okura, T. Crystallization and sodium-ion conduction properties of glass-ceramic solid solutions of Na₅FeSi₄O₁₂ and Na₄ZrSi₄O₁₂. *Funct. Mater. Lett.* **2021**, *14*, 2141001. [[CrossRef](#)]
27. Gandi, S.S.; Gandi, S.; Madduluri, V.R.; Katari, N.K.; Dutta, D.P.; Ravuri, B.R. Na_{3+x}[Cr_xTi_{2-x}(PO₄)₃] glass-ceramic electrolyte: Ionic conductivity and structural correlations for different heat treating temperatures and time schedules. *Ionics* **2019**, *25*, 4179–4188. [[CrossRef](#)]
28. Zhu, Y.; Li, L.; Li, C.; Zhou, L.; Wu, Y. Na_{1+x}Al_xGe_{2-x}P₃O₁₂ (x = 0.5) glass-ceramic as a solid ionic conductor for sodium ion. *Solid State Ionics* **2016**, *289*, 113–117. [[CrossRef](#)]
29. Kubuki, S.; Osouda, K.; Ali, A.S.; Khan, I.; Zhang, B.; Kitajou, A.; Okada, S.; Okabayashi, J.; Homonnay, Z.; Kuzmann, E.; et al. ⁵⁷Fe-Mössbauer and XAFS studies of conductive sodium phospho-vanadate glass as a cathode active material for Na-ion batteries with large capacity. *J. Non-Cryst. Solids* **2021**, *570*, 120998. [[CrossRef](#)]
30. Khan, I.; Zhang, B.; Matsuda, K.; Bingham, P.A.; Kitajou, A.; Inoishi, A.; Okada, S.; Yoshioka, S.; Nishida, T.; Homonnay, Z.; et al. Development of electrically conductive ZrO₂-CaO-Fe₂O₃-V₂O₅ glass and glass-ceramics as a new cathode active material for Na-ion batteries with high performance. *J. Alloys Compd.* **2022**, *899*, 163309. [[CrossRef](#)]
31. Li, R.; Guan, C.; Bian, X.; Yu, X.; Hu, F. NaV₆O₁₅ microflowers as a stable cathode material for high-performance aqueous zinc-ion batteries. *RSC Adv.* **2020**, *10*, 6807–6813. [[CrossRef](#)] [[PubMed](#)]
32. Hu, F.; Jiang, W.; Dong, Y.; Lai, X.; Xiao, L.; Wu, X. Synthesis and electrochemical performance of NaV₆O₁₅ microflowers for lithium and sodium ion batteries. *RSC Adv.* **2017**, *7*, 29481–29488. [[CrossRef](#)]
33. Wei, D.; Wang, H.; Feng, X.; Chueh, W.-T.; Ravikovitch, P.; Lyubovsky, M.; Li, C.; Takeguchi, T.; Haller, G.L. Synthesis and characterization of vanadium-substituted mesoporous molecular sieves. *J. Phys. Chem. B* **1999**, *103*, 2113–2121. [[CrossRef](#)]

34. Kong, F.; Sun, D.; Rao, Y.; Zhang, R.; Chen, Z.; Wang, D.; Yu, X.; Jiang, H.; Li, C. Order-disorder transition in amorphous Vanadium-Phosphorus-Lithium cathode of lithium ion battery. *Appl. Surf. Sci.* **2022**, *573*, 151490. [[CrossRef](#)]
35. Ibrahim, A.; Kubo, K.; Watanabe, S.; Shiba, S.; Khan, I.; Zhang, B.; Homonnay, Z.; Kuzmann, E.; Pavić, L.; Santić, A.; et al. Enhancement of electrical conductivity and thermal stability of Iron- or Tin- substituted vanadate glass and glass-ceramics nanocomposite to be applied as a high-performance cathode active material in sodium-ion batteries. *J. Alloys Compd.* **2023**, *930*, 167366. [[CrossRef](#)]
36. Nagaraju, G.; Chandrappa, G.T. Solution phase synthesis of $\text{Na}_{0.28}\text{V}_2\text{O}_5$ nanobelts into nanorings and the electrochemical performance in Li battery. *Mater. Res. Bull.* **2012**, *47*, 3216–3223. [[CrossRef](#)]
37. Ibrahim, A.; Arita, Y.; Ali, A.S.; Khan, I.; Zhang, B.; Razum, M.; Pavić, L.; Santić, A.; Homonnay, Z.; Kuzmann, E.; et al. Impact of adding Fe ions on the local structure and electrochemical performance of $\text{P}_2\text{O}_5\text{-V}_2\text{O}_5$ glass and glass ceramics used as a cathode in LIBs. *J. Phys. Chem. Solids* **2023**, *179*, 111391. [[CrossRef](#)]
38. Douvartzides, S.L.; Charisiou, N.D.; Papageridis, K.N.; Goula, M.A. Green diesel: Biomass feedstocks, production technologies, catalytic research, fuel properties and performance in compression ignition internal combustion engines. *Energies* **2019**, *12*, 809. [[CrossRef](#)]
39. Tanaka, T.; Yamashita, H.; Tsuchitani, R.; Funabiki, T.; Yoshida, S. X-ray absorption (EXAFS/XANES) study of supported vanadium oxide catalysts. Structure of surface vanadium oxide species on silica and γ -alumina at a low level of vanadium loading. *J. Chem. Soc. Faraday Trans.* **1988**, *84*, 2987–2999. [[CrossRef](#)]
40. Wong, J.; Lytle, F.W.; Messmer, R.P.; Maylotte, D.H. K-edge absorption spectra of selected vanadium compounds. *Phys. Rev. B* **1984**, *30*, 5596–5610. [[CrossRef](#)]
41. Renka, S.; Pavić, L.; Tricot, G.; Mošner, P.; Koudelka, L.; Mogaš-Milanković, A.; Šantić, A. A significant enhancement of sodium ion conductivity in phosphate glasses by addition of WO_3 and MoO_3 : The effect of mixed conventional–conditional glass-forming oxides. *Phys. Chem. Chem. Phys.* **2021**, *23*, 9761–9772. [[CrossRef](#)]
42. Pavić, L.; Šantić, A.; Nikolić, J.; Mošner, P.; Koudelka, L.; Pajić, D.; Mogaš-Milanković, A. Nature of mixed electrical transport in $\text{Ag}_2\text{O-ZnO-P}_2\text{O}_5$ glasses containing WO_3 and MoO_3 . *Electrochim. Acta* **2018**, *276*, 434–445. [[CrossRef](#)]
43. Marijan, S.; Razum, M.; Klaser, T.; Mošner, P.; Koudelka, L.; Skoko, Ž.; Pisk, J.; Pavić, L. Tailoring structure for improved sodium mobility and electrical properties in $\text{V}_2\text{O}_5\text{-Nb}_2\text{O}_5\text{-P}_2\text{O}_5$ Glass(es)-(Ceramics). *J. Phys. Chem. Solids* **2023**, *181*, 111461. [[CrossRef](#)]
44. Mansour, A.N.; Smith, P.H.; Baker, W.M.; Balasubramanian, M.; McBreen, J. In situ XAS investigation of the oxidation state and local structure of vanadium in discharged and charged V_2O_5 aerogel cathodes. *Electrochim. Acta* **2002**, *47*, 3151–3161. [[CrossRef](#)]
45. Aoyagi, T.; Fujieda, T.; Toyama, T.; Kono, K.; Takamatsu, D.; Hirano, T.; Naito, T.; Hayashi, Y.; Takizawa, H. Electrochemical properties and in-situ XAFS observation of $\text{Li}_2\text{O-V}_2\text{O}_5\text{-P}_2\text{O}_5\text{-Fe}_2\text{O}_3$ quaternary-glass and crystallized-glass cathodes. *J. Non-Cryst. Solids* **2016**, *453*, 28–35. [[CrossRef](#)]
46. Baddour-Hadjean, R.; Huynh, L.T.N.; Emery, N.; Pereira-Ramos, J. Lithium insertion in α' - NaV_2O_5 : Na-pillaring effect on the structural and electrochemical properties. *Electrochim. Acta* **2018**, *270*, 224–235. [[CrossRef](#)]
47. Baddour-Hadjean, R.; Bach, S.; Emery, N.; Pereira-Ramos, J.P. The peculiar structural behaviour of β - $\text{Na}_{0.33}\text{V}_2\text{O}_5$ upon electrochemical lithium insertion. *J. Mater. Chem.* **2011**, *21*, 11296–11305. [[CrossRef](#)]
48. Wang, X.; Liu, Q.; Wang, H.; Jiang, D.; Chang, Y.; Zhang, T.; Zhang, B.; Mou, H.; Jiang, Y. PVP-modulated synthesis of $\text{NaV}_6\text{O}_{15}$ nanorods as cathode materials for high-capacity sodium-ion batteries. *J. Mater. Sci.* **2016**, *51*, 8986–8994. [[CrossRef](#)]
49. Cai, Y.; Zhou, J.; Fang, G.; Cai, G.; Pan, A.; Liang, S. $\text{Na}_{0.282}\text{V}_2\text{O}_5$: A high-performance cathode material for rechargeable lithium batteries and sodium batteries. *J. Power Sources* **2016**, *328*, 241–249. [[CrossRef](#)]
50. Rai, A.K.; Anh, L.T.; Gim, J.; Mathew, V.; Kim, J. Electrochemical properties of Na_xCoO_2 ($x \sim 0.71$) cathode for rechargeable sodium-ion batteries. *Ceram. Int.* **2014**, *40*, 2411–2417. [[CrossRef](#)]
51. He, H.; Jin, G.; Wang, H.; Huang, X.; Chen, Z.; Sun, D.; Tang, Y. Annealed NaV_3O_8 nanowires with good cycling stability as a novel cathode for Na-ion batteries. *J. Mater. Chem. A* **2014**, *2*, 3563–3570. [[CrossRef](#)]
52. Köhler, J.; Makihara, H.; Uegaito, H.; Inoue, H.; Toki, M. LiV_3O_8 : Characterization as anode material for an aqueous rechargeable Li-ion battery system. *Electrochim. Acta* **2000**, *46*, 59–65. [[CrossRef](#)]
53. Gourier, D.; Tranchant, A.; Baffier, N.; Messina, R. EPR study of electrochemical lithium intercalation in V_2O_5 cathodes. *Electrochim. Acta* **1992**, *37*, 2755–2764. [[CrossRef](#)]
54. Kang, H.; Liu, Y.; Shang, M.; Lu, T.; Wang, Y.; Jiao, L. NaV_3O_8 nanosheet@polypyrrole core-shell composites with good electrochemical performance as cathodes for Na-ion batteries. *Nanoscale* **2015**, *7*, 9261–9267. [[CrossRef](#)]
55. Zhu, L.; Li, W.; Xie, L.; Yang, Q.; Cao, X. Rod-like NaV_3O_8 as cathode materials with high capacity and stability for sodium storage. *Chem. Eng. J.* **2019**, *372*, 1056–1065. [[CrossRef](#)]
56. Zhu, L.; Li, W.; Yu, Z.; Xie, L.; Cao, X. Synthesis and electrochemical performances of $\text{LiV}_3\text{O}_8/\text{poly}(3, 4\text{-ethylenedioxythiophene})$ composites as cathode materials for rechargeable lithium batteries. *Solid State Ion.* **2017**, *310*, 30–37. [[CrossRef](#)]

Disclaimer/Publisher’s Note: The statements, opinions and data contained in all publications are solely those of the individual author(s) and contributor(s) and not of MDPI and/or the editor(s). MDPI and/or the editor(s) disclaim responsibility for any injury to people or property resulting from any ideas, methods, instructions or products referred to in the content.